A long-lived Indian Ocean slab: Deep dip reversal induced by the African LLSVP

Huilin Wang[a,*], Yaoyi Wang[a,b,**], Michael Gurnis[a], Sabin Zahirovic[c], Wei Leng[b]

[a] Seismological Laboratory, California Institute of Technology, Pasadena, CA, 91125 United States

[b] School of Earth and Space Sciences, University of Science and Technology of China, Hefei, China

[c] Basin GENESIS Hub and EarthByte Group, School of Geosciences, University of Sydney, NSW 2006, Australia

[*] *Now at: Institute of Geophysics, MOE Key Laboratory of Fundamental Physical Quantities Measurement, School of Physics, Huazhong University of Science and Technology, Wuhan, China*

[**] *Now at*: Department of Geology, University of Illinois, Urbana, IL 61801, United States

Correspondence to:

Huilin Wang

huilin@gps.caltech.edu

ABSTRACT

A slab-like high seismic velocity anomaly (referred as SEIS) has been inferred beneath the central-southern Indian Ocean in a recent tomographic inversion. Although subduction has previously been suggested regionally by surface observations, the new inversion is consistent with a north-dipping slab extending from the upper mantle to the core mantle boundary (CMB). We propose that SEIS anomaly originated from an oceanic plate in the Paleo-Tethys that was consumed by a south-dipping intra-oceanic subduction zone during the Triassic and Jurassic period. SEIS challenges traditional concepts of the dynamics of slab decent by its relatively shallow depths and a present-day polarity opposite to the geometry of subduction. Geodynamic models show the upwelling mantle flow exerted by a thermochemical pile can hold and stagnate the descending SEIS slab at shallow depths for more than 100 Myr. The spatial distribution of resistance from the upwelling mantle flow can reverse the slab dip, producing a structure consistent with seismic inversions yet starting with a plate tectonic reconstruction consistent with the geology constraining the Tethyan tectonic domain. The results suggest that slabs can descend through the lower mantle at rates substantial lower than 1 cm/yr, and even reverse their polarity through interactions with background mantle flow.

1. Introduction

A slab-like, high seismic velocity anomaly has been interpreted from seismic tomography of the mantle beneath the southern Indian Ocean recently, referred to as the southeast Indian slab (SEIS) (Simmons et al., 2015; Fig. 1). Although high seismic velocities had been previously inferred (see Fig. S1), a new global Earth model (LLNL-G3D-JPS) (Simmons et al., 2015) recovers a massive high-velocity anomaly, which regionally can display a slab-like structure, with a northward dipping feature from the upper mantle toward the core mantle boundary (CMB). The most slab-like cross section resides in a corridor between the Kerguelen Plateau and Java in Indonesia (Fig. 1a).

The presence of a slab beneath the Indian Ocean has long been suspected. Chase

(1979) argued that the band of geoid lows starting south of Indian, passing through Siberia, over North America, down the western Atlantic and through the Ross Sea in Antarctica before connecting up again with the Indian geoid low, are generated by mass anomalies at about 1,200 km depth. Based on the position of the geoid lows and the paleo-position of Mesozoic subduction zones, Chase and Sprowl (1983) suggested that slabs in the lower mantle were responsible for the geoid lows, including a slab suggested beneath the Indian Ocean. Spasojevic et al. (2010) noted an inverted structure in the central Indian Ocean mantle with higher shear velocities below 2,000 km and lower velocities above 1,000 km. Ghosh et al. (2017) suggested that the low-density materials at ~300-900 km depth are responsible for the Indian Ocean geoid low. The low-density materials could be entrained plumes from the edge of the African large low-shear-velocity province (LLSVP) (Nerlich et al., 2016) or resulted from dehydration of Mesozoic slab in the lower mantle (Spasojevic et al., 2010).

Despite seismic inversions and geoid interpretations pointing to the possibility of Mesozoic subduction in the central Indian Ocean, Simmons et al. (2015) noted the lack of Mesozoic plate reconstructions displaying subduction zones with a northward polarity. In contrast, evidence for the Mesozoic tectonic evolution of the eastern Tethyan region indicate a south-dipping subduction zone and an overall northward plate motion through continued slab rollback. Independent data suggest that the Lhasa terrane has Gondwana tectonic affinities and drifted northward over a south-dipping subduction zone during Triassic to Jurassic period (e.g., Li et al., 2016; Zhu et al., 2011a). The south-dipping subduction zone with a northward-retreating hinge could migrate across and consume the Paleo-Tethyan oceanic plate(s) (see details in Section 2). The present-day seismic high-velocity anomaly beneath the Indian Ocean therefore may capture the consumed Paleo-Tethyan oceanic plate(s), and hence document the opening of the successor Meso-Tethys. When examining the morphology of the SEIS anomaly with the Paleo-Tethyan tectonics, two questions emerge. First is the inconsistency between southward subduction polarity within the Paleo-Tethyan ocean and the north-dipping SEIS anomaly. A south-dipping subduction zone that retreats northward is expected to produce a south-dipping slab in the mantle, but the SEIS anomaly has a north-dipping structure.

The second question is how the slab stagnated above or at the 660 km discontinuity for more than 145 Myr. Previous studies estimated the globally average descending rate of slabs is 1.2 ± 0.3 cm/yr in the lower mantle (van der Meer et al., 2009) and 1.3 ± 0.3 cm/yr for the whole mantle (Butterworth et al., 2014). Using a descent velocity of 1.3 cm/yr, the slab would sink to ~1900 km depth from the Jurassic to present, which is much deeper than the shallow portion of the SEIS anomaly. The transition zone can temporarily trap a slab resulting from trench retreat (e.g., Christensen, 1996), phase transitions (e.g., Christensen and Yuen, 1985), viscosity increase (e.g., Gurnis and Hager, 1988), slab strength variation (e.g., Čížková et al., 2002) and/or slab temperature variation (King et al., 2015). But as the slab penetrates into the lower mantle, the slab is usually reshaped by the long-term resistive stresses at the transition zone, which results in a complex slab morphology in the lower mantle (Zhong and Gurnis, 1995; Christensen, 1996). However, the SEIS anomaly appears to have a simple dipping structure.

The newly-found SEIS anomaly is inconsistent with traditional concepts of a sinking slab. The dynamic of subducted slabs is usually considered to be dominated by its negative thermal buoyancy. Therefore, the subducted slab is anticipated to sink largely vertically with a rate proportional to its negative buoyancy and inversely proportional to the background mantle viscosity. Increasing studies noted that this assumption is oversimplified and the sinking rate may vary significantly among different regions (e.g., Jarvis and Lowman, 2007; Schellart et al., 2009; Zahirovic et al., 2014). Below the southern Indian Ocean, the SEIS anomaly is lying above the E-W orientated limb of the African LLSVP (Fig. 1). As one of two largest low seismic velocity provinces (the other one below mid-Pacific) in the lower mantle, the African LLSVP occupies an area of ~1.8×10^7 km^2 and extends at least 1,300 km above the CMB (e.g., Dziewonski, 1984). The low seismic velocities are characterized by anti-correlation between the bulk-sound velocity and shear velocity below 2,000 km depth, suggesting compositionally distinct characteristics (Masters et al., 2000). The compositional difference may impose a higher density and/or viscosity on the LLSVPs compared to ambient mantle (e.g., Ishii and Tromp, 1999; McNamara and Zhong, 2004; Lau et al., 2017), and results in spatial stability of the LLSVPs for the post-Pangea timeframe over the last 200 Myr. However, the mantle in the vicinity of the LLSVPs is not stable, and the high temperatures make the edges of LLSVPs long-lived sources of upwelling thermal plumes. For example, the upwelling mantle flow above the African LLSVP is suggested to have caused the unusual large-scale Cenozoic uplift and support the broad topography high in southern Africa (Hager et al., 1984; Nyblade and Robinson, 1994; Lithgow-Bertelloni and Silver, 1998; Gurnis et al., 2000a). The Pacific LLSVP may have imparted a strong upward vertical force on the descending Tonga slab (Gurnis et al., 2000b). Elevated southern Africa and the enigmatic stress field of the Tonga slab indicate that the upward mantle stress is significant, but how the upwelling flow influences the dynamics of subducted slabs is not known.

In this study, we first review the geological data of the Mesozoic plate motion and present the scenario of south-dipping subduction with northward retreating hinge that consumed Paleo-Tethyan plate(s). We then use numerical models to investigate the possibility of a south-dipping subduction zone producing the present-day north-dipping seismic anomaly. We focus on the interaction between the subducted Mesozoic slab and the upwelling flow from the African LLSVP, and trace the morphology of the subducted slab. Using geodynamic models, we show that upwelling mantle flow can hold the slab, and in some cases entirely flip the slab polarity. This provides a solution for the discrepancies between the Paleo-Tethyan plate motion inferred from geology and the observed seismic anomaly. More generally, we show the importance of upwelling mantle flow on reshaping adjacent subducted slabs.

2. Geological constraints

The Cenozoic plate motion in the Indian Ocean region is well constrained by the magnetic lineations of the South East Indian Ridge and South West Indian Ridge as well as paleomagnetism of the Indian subcontinent (Zahirovic et al., 2016). Before the Cenozoic, the Indian continent separated from East Gondwanaland in the Early Cretaceous and traveled northward across the Neo-Tethys Ocean until accreting to Eurasia in the Eocene (Hall, 2012). The Neo-Tethyan plate, which represented the oceanic gateway between India and Eurasia, subducted at the southern margin of Eurasia (Seton et al., 2012), probably with a secondary intra-oceanic subduction zone that extended from the eastern Mediterranean to Indonesia (Hafkenscheid et al., 2006;

Zahirovic et al., 2012). The shape and distribution of the consumed Neo-Tethyan plate has been investigated and constrained by seismic and geodynamic studies, primarily at mid-mantle depths in the Northern Hemisphere and near-equatorial latitudes (van der Voo et al., 1999; Zahirovic et al., 2012; Nerlich et al., 2016). Prior to the Cretaceous, with the lack of preserved seafloor spreading histories, the plate motions are more ambiguous. However, there are a few lines of evidence for the Paleo- and Meso-Tethys plate tectonic evolutions.

Zircon age spectra and Hf isotopic data suggest that the Lhasa terrane has Gondwana (likely NW Australian shelf) tectonic affinities (Burrett et al., 2014; Zhu et al., 2011b). Paleomagnetic data syntheses suggest that the Lhasa terrane drifted away from the Gondwanaland in the Late Triassic and moved northward from ~15°S to ~25°N until colliding with Qiangtang on Eurasia in the Early Cretaceous, which forms present-day Tibet (Li et al., 2005; Li et al., 2016; Fig. 2a). The northward motion of the Lhasa terrane is consistent with other Tethyan terranes that have been accreted to southern Eurasia or Southeast Asia. The Lhasa terrane also records continuous subduction-related magmatism from at least ~215 Ma, which approximately represents the onset of northward drift, to ~150 Ma (Zhu et al., 2011a; Fig. 2b). The magmatic history of Lhasa displays a progressive younging from the south (started from ca. 215 Ma) to the north (started from ca. 134 Ma) (Zhu et al., 2011a; Fig. 2b). Zhu et al. (2011a) interpreted this northward migration of magmatism as the rollback of continuous south-dipping subduction at the northern margin of the Lhasa terrane. The northward retreating of subduction hinge opened the Meso-Tethys from ~200 Ma as a back-arc basin (Fig. 2b). After the Lhasa terrane accreted onto Eurasia, the Meso-Tethyan oceanic plate started to subduct at a north-dipping subduction zone along the southern margin of Lhasa.

A north-dipping subduction zone may have been contemporaneously active along southern Eurasia within the Paleo-Tethyan plate. However, this north-dipping subduction zone would have had a limited lifespan and would have been interrupted by the northward migration of the Lhasa terrane. Simmons et al. (2015) also noted that the southward hinge retreating scenario requires Australia to be located further south than the scenarios presented in most plate reconstructions, further supporting the possibility that this slab represents an older subduction system than the Cretaceous to Eocene Neo-Tethyan system during which Australia was moving northward towards Eurasia (Gibbons et al., 2015).

The paleomagnetic, geochronological, and petrological constraints indicate a northward motion of Lhasa and a southward polarity of a Tethyan subduction zone during the Triassic to Jurassic period. As other subducted Mesozoic slabs in the deep mantle detected by seismic surveys (e.g., the Farallon plate below North America), the SEIS anomaly inferred in the new seismic image could be the consumed Paleo-Tethyan plate.

3. Insights from two-dimensional models

There is little work on how a subducted slab descends through the mantle in the presence of a mantle structure with characteristics appropriate for an LLSVP. Before using spherical models of mantle convection with explicit plate reconstructions, a brief consideration of the factors governing slab descent is appropriate. We carried out 37 two dimensional, time-dependent computations (see Supplementary Material for details) with the primary factors determining the descent rate, including the lower mantle viscosity,

viscosity contrast across the slab, lithosphere age before subduction, slab geometry (slab position with respect to mantle upwelling and dip), strength of the phase transition at 660 km depth and the characteristics of the thermochemical pile (the modeled LLSVP), including its Rayleigh number, ratio of chemical to thermal differential density, and background viscosity. Results from two-dimensional models must be used carefully as the three-dimensional configuration could prove to be key and the along strike length of the ancient Indian Ocean slab could be longer or shorter than the width of the LLSVP.

Many of the results are self-evident from the wide body of work on mantle convection (Schubert et al., 2001), such as the inverse relation between descent rate and lower mantle viscosity and the dependence of descent rate on the net buoyancy of the thermochemical pile, the age of the lithosphere prior to subduction, and the Clapeyron slope of the 660 km discontinuity. However, two factors did produce results that were initially unexpected. First, the initial dip angle of the slab, either to the south and/or to the north, had a substantial influence on the final dip angle. When the slab was displaced from the center of the pile, the northern dip of the slab descended at a larger rate than the southern edge, such that in time the slab became nearly vertical. In some cases, because the models were two dimensional, the slab could overturn especially for those cases with net positive buoyancy for the pile. The end result could be a slab that dips to the south, not north. However, if the slab initially dipped to the south, as implied by our preferred reconstructions of the Indian Ocean, we found a range of cases in which the slab eventually developed an apparent dip down to the north (Fig. 3). In these cases, the slab descended at a normal rate to the north but a slower rate over the chemical pile. We found cases in which the slab could approximately blanket the chemical pile.

The ambient or pre-exponential factor to the viscosity law for the material composing the chemical pile also strongly influenced the descent of the slab. Using the idea that the material could have been primordial and composed of material with a substantially larger grain size (Solomatov and Reese, 2008), the pile could have a high viscosity despite its high temperature, essentially overcoming of the normal temperature dependence of viscosity. In these cases (Fig. 3), the descent of the slab could slow down such that after several hundred million years the slab still remains on top of the pile.

4. Global mantle convection models

4.1 Methods

To investigate the dynamic of the SEIS slab below Indian Ocean, we construct global mantle convection models in a spherical domain with paleo-geographical constraints. The equations of conservation of mass, momentum and energy under the Boussinesq approximation are solved using the finite element code *CitcomS* (Zhong et al., 2000). All models are run from 160 Ma to the present. This Late Jurassic age is chosen as it represents the late stage of Paleo-Tethyan closure and suturing of Lhasa with Eurasia (Yan et al., 2016), and approximates the time from which the Paleo-Tethyan slab is likely to be freely sinking in the mantle. Plate reconstructions (Zahirovic et al., 2016) with 1 Myr time intervals are incorporated in the surface velocity fields; the thermal structure of the lithosphere and the shallow portion of subducted slabs (above 350 km depth) are progressively assimilated (Bower et al., 2015). As the slab subducts to depths greater than 350 km, it progressively merges with the dynamically evolving mantle convection. The thermal structure of the oceanic lithosphere is simulated based on reconstructed seafloor ages and a half-space cooling model, and the continental thermal structure is based on tectonothermal ages of terranes (Flament et al., 2014).

The mantle flow model has 12 caps, each with 128×128×64 elements, resulting in ~50 km resolution at the surface and ~26 km at the CMB. Refinement is used in the radial direction, providing the highest resolution of 18 km near the top and bottom boundaries and a lowest resolution of ~90 km in the mid-mantle. We prescribe an isothermal boundary at the top surface (non-dimensional temperature T=0) and a free slip and isothermal boundary condition at the CMB (T=1). All materials have temperature- and composition-dependent density. The viscosity is a function of temperature, depth and composition (Fig. 4; see detailed in Supplementary Material). Detailed model parameters are listed in Table 1.

We aim to investigate the interaction between subducted Mesozoic slab and the African thermochemical pile. As we explore different Paleo-Tethyan plate motions which are not yet incorporated into the current generation of plate reconstructions, we place a synthetic slab in the mantle below southern Indian Ocean region as an initial condition (Fig. 5). The slab extends between depths of 350 and 1,200 km, covering an area of 3,500 km (in EW direction) × 4,000 km (in NS direction). The slab dips southward, which is assumed to result from a south-dipping subduction zone that retreated northeastward in the Jurassic to Triassic period according to previous studies (e.g., Zhu et al., 2011a; Li et al., 2004; Li et al., 2016). The thermal structure of the slab is created using a Gaussian function and the buoyancy corresponds to an initial 40- to 80-Myr-old oceanic lithosphere (the initial age being a free parameter). The temperature across slab boundaries is smooth and gradually increased to the ambient mantle temperature (T=0.5).

We prescribe two thermochemical piles residing at the positions for the African and Pacific LLSVPs inferred from tomographic images (Fig. 5). For simplicity, we define a height of 600 km for the thermochemical piles. The interiors of the pile structures have a temperature of T=0.8, which is 60% higher than ambient. Tracers are used to represent the synthetic thermochemical piles, in order to track the density and/or viscosity variation due to the compositional difference. The African and Pacific piles are 100 kg/m^3 denser and 10 times higher in viscosity than the ambient mantle in order to stabilize these features in the lowermost mantle.

4.2. Results

Mantle convection is influenced by both the low-temperature downgoing slabs and the upwelling mantle flow sourced from the hot thermochemical piles (Model 1; Fig. 6). The updraft flow from the African pile holds and uplifts the southern portion of the synthetic slab. The northern slab, without the thermochemical pile lying below, sinks vertically driven by its negative buoyancy. As a result of the unevenly distributed resistance stresses from the mantle flow, the slab gradually flips in the mantle. Since ~70 Ma, the dip direction of the slab reverses from southward to northward. The eastern Tethyan subduction zone during the Cretaceous and subduction zones around Indonesia feed additional subducted slabs into the mantle below ~25°S-0°N (the northern part of the cross section in Fig. 6). The accumulated negative buoyancy pushes the slab to the deepest mantle. At 0 Ma, the slabs in the south still resides at ~400 km depth in the upper mantle, while the slabs in the north have already reached the CMB (Fig. 7). The geometry of the slab materials is generally consistent with the SEIS anomaly in the LLNL tomography image (Fig. 8; Simmons et al., 2015).

The African thermochemical pile gradually upwells to mid-mantle depths (~1,200 km) in the Model 1. Faster than the thermochemical pile, the hot mantle initially surrounding the African pile convects to the top of the thermochemical pile and ascends into the upper mantle. This results in a sharp thermal transition at the side boundaries of the African pile. Meanwhile, the African pile has been pushed ~15° southward by the sinking slabs by 70 Ma, followed by a period of stability above the CMB. In the cross section (Fig. 6), the initial “square-shaped” thermochemical pile gradually evolves into a bell-like structure that slightly tilts northward.

We test two end-member cases in which there is either no inserted slab or no African pile (Table 2). Model 2 tests the case without the slab insertion below the central Indian Ocean (Fig. S3a). The other model parameters are identical to that in the Model 1. Subduction arises as it does in Zahirovic et al. (2016) with the subducted slabs mainly residing beneath the Australia region. In cross-section, the Mesozoic subducted slab accumulates beneath the NW shelf of Australia between mid- to lower-mantle depths at 0 Ma. The model result confirms that the current generation of plate reconstructions cannot generate the SEIS-like anomaly. The African pile below the southern Indian Ocean is pushed westward by the mantle flow generated by the eastern Tethyan subduction zone. In Model 3, the African pile is not imposed (Fig. S3b), the slab sinking is dominated by negative buoyancy and so is not impeded during its descent. The transition zone temporarily traps the northern portion of the slab; thus the slab dip steepens with time but the direction of dip remains the same.

A series of additional models are computed to investigate the effects of the slab buoyancy, viscosity jump and Clapeyron slope at the 660 km discontinuity, as well as the density and viscosity contrast of the thermochemical piles. If the inserted slab is 40 Myr older than in Model 1, the slab is thicker and denser (Model 4; Fig. S3c). Even though the slab has more negative buoyancy, the slab still flips through the flow induced by the hot mantle sourced from the African pile. The viscosity increase and delay of the phase change at 660 km discontinuity can reduce slab descent. We test the case with a modest, factor of 30, increase in the viscosity at 660 km discontinuity (Model 5; Fig. S3d). The motion of the descending slab and upwelling hot mantle are both more rapid compared to that found in Model 1. The upwelling mantle flow reverses the slab earlier in this case. At 0 Ma, the shallow portion of African thermochemical pile sits directly below the 660 km discontinuity, and a large portion of the Mesozoic slab rests above the CMB. The overall dip of the slab in the mid-mantle is approximately vertical. If the Clapeyron slope of the ringwoodite transformation is zero (Model 6; Fig. S3e), the slab descends at a slightly larger rate into the lower mantle in this case.

The physical properties of the African and Pacific thermochemical piles are poorly known. If the viscosity of thermochemical piles is lower than in Model 1 by a factor of 10, the thermochemical pile upwells more rapidly with narrower widths as “hot sheets” (Model 7; Fig. S4a). At 0 Ma, the top of thermochemical pile is positioned in the upper mantle at ~400 km depth. In Model 8, the thermochemical piles are 125 kg/m^3 denser than ambient mantle (Fig. S4b). The higher density makes the African pile more stable at the CMB, with a flatter and more defined outer shape compared to that in Model 1.

5. Discussion and conclusions

A substantial high seismic velocity anomaly is found beneath the central-southern Indian Ocean, characterized by a northward dipping feature from the upper mantle to the CMB, lying above the African LLSVP (Simmons et al., 2015; Fig. 1). The SEIS anomaly is likely to be a residual Tethyan plate consumed in the Mesozoic. However, the shape of the SEIS anomaly and the inferred Tethyan plate history are controversial (Fig. 2). This study designs numerical models to investigate the interaction between thermochemical piles and subducted slabs. Models show that the upwelling flow from the thermochemical pile imposes a sizeable upward stress on the overlying slab, resulting in a much lower slab descent rate. The slab above the upwelling flow can stagnate at shallow depths for more than one hundred million years (Fig. 6). For slabs more distal from the thermochemical pile, the negative buoyancy drives the slab to sink sub-vertically. As a result, a slab, which was initially south-dipping and lying across the African pile, gradually flips and reverses its polarity by the unevenly distributed resistance stress in the viscous mantle. At present, the predicted slab exists in a northward polarity extending from the upper mantle to the CMB, which is generally consistent with the observed SEIS anomaly. Models demonstrate that the SEIS anomaly could be a fragment of the Paleo-Tethyan plate, which was subducted at a south-dipping, intra-oceanic subduction zone during Triassic to Jurassic times, consistent with the magmatism and paleomagnetic records on the Lhasa terrane (Zhu et al., 2011a; Li et al., 2004; Li et al., 2016). Detailed requirements for the subducted slab(s) (e.g., spatial coverage and geometry) for matching the seismic anomalies and their implications for the Tethyan oceanic tectonics need to be investigated in future.

Compared to previous studies that use simple models and/or assume a constant slab descent rate, this study investigates the slab motion in the region where the upwelling mantle flow is active (e.g., above LLSVPs). We demonstrate that the slab evolution can strongly depend on the background mantle flow. Above the LLSVPs, which are the largest heat anomalies in the mantle, the thermal plumes can push through the viscous mantle and rise from the deepest mantle to contribute to uplift at Earth's surface (e.g., Hager et al., 1984; Torsvik et al., 2010; Gurnis et al., 2000a). If a slab descends into the LLSVP, the upwelling thermal plumes can hold, stagnate and reshape the slab. We have carried out a series of 2D and global models to test the variation of modeling parameters within a reasonable range (Tables 2 and S2). Some differences are shown in the present-day morphology of the slab (Figs. 2 and 8), but the upwelling flow plays the first-order role in flipping a slab in the mantle. The models show that the background stress induced by the mantle flow can complicate interpretations of slab polarity and depth. Therefore, we suggest that further evaluation of seismic image in the mantle needs to apply a geodynamic flow model to forward predict the synthetic seismic structure from plate reconstructions.

The African and Pacific LLSVPs are suggested to be thermally and chemically distinct from seismic data (e.g., Su and Dziewonski, 1997), and therefore they are likely to have a different density and viscosity than the surrounding mantle. Many studies suggest that the interior density in LLSVPs is higher than that of ambient mantle (e.g., Ishii and Tromp, 1999; Lau et al., 2017), but the viscosity is poorly constrained. Models show that a high viscosity can stabilize the thermochemical piles in the deepest mantle (e.g., Model 1). Otherwise, if the thermochemical piles have the same viscosity relationship as the lower mantle (Model 7), then the hot piles are easily entrained as short wavelength volumes that upwell to the upper mantle within ~150 Myr. Koelmeijer et al. (2017) recently proposed the LLSVPs are less dense than the surrounding mantle based on the splitting Stoneley modes of free oscillations. Even through this study noted the possibility of a ~100-km-thick iron-rich denser layer at the base, the buoyant portion of the LLSVPs could require an even higher viscosity for maintaining the layered-density structure and anchoring the LLSVPs to the CMB. From a compositional perspective, if the LLSVPs are strong and do not participate in convection, then they can remain compositionally distinct from the rest of the convecting mantle for long periods of time. The high viscosity of the LLSVPs could be caused by large grain sizes inherited from a primordial mantle or through Ostwald ripening. Solomatov and Reese (2008) postulated that the viscosity variations caused by grain size variations in the mantle can be at least two orders of magnitude. Mixing of heterogeneities can be significantly delayed if the viscosity of the heterogeneities is larger than that of the surrounding mantle. This could allow the chemical heterogeneities to survive for billions of years despite ongoing mantle convection.

The convective mantle flow caused by the downgoing slab also modifies the thermal structure of thermochemical piles. The convective mantle flow advects the hot mantle around the thermochemical piles. If the convective flow erodes the boundaries of the LLSVPs faster than thermal diffusion, the thermal boundary of the LLSVPs gradually sharpens. Because subduction zones and downwelling slabs dominate to the north of the African LLSVP, our models predict the northern side of the African LLSVP could be sharper than the southern side.

This study investigates the interaction between a subducted slab and upwelling mantle flow. We propose that the north-dipping SEIS anomaly observed in the seismic observations could be Paleo-Tethyan oceanic lithosphere that subducted at a south-dipping subduction zone. The upwelling flow exerted from the African LLSVP can reverse the slab polarity and stagnate the slab at shallow depths for more than one hundred million years. More broadly, our models show that the influence of the upwelling buoyant mantle on slab dynamics can be more significant than recognized earlier.

Acknowledgements. We thank two anonymous reviewers for their invaluable comments and suggestions. We also thank Nathan Simmons for earlier discussions on the origin of the SEIS and Kara Matthews for discussions of Tethyan reconstructions. HW and MG were supported by the National Science Foundation through EAR-1600956 and EAR-1645775 and by Statoil ASA. YW participated through the Visiting Undergraduate Research Program (VURP) at Caltech. SZ was supported by the Australian Research Council through IH130200012. The original *CitcomS* code is obtained from Computational Infrastructure for Geodynamics (http://geodynamics.org).

References

Bower, D.J., Gurnis, M. and Flament, N., 2015. Assimilating lithosphere and slab history in 4-D Earth models. Physics of the Earth and Planetary Interiors, 238, pp.8-22.

Burrett, C., Zaw, K., Meffre, S., Lai, C., Khositanont, S., Chaodumrong, P., Udchachon, M., Ekins, S., Halpin, J.A., 2014. The configuration of Greater Gondwana-Evidence from LA ICPMS, U-Pb geochronology of detrital zircons from the Palaeozoic and Mesozoic of Southeast Asia and China. Gondwana Res. 26, 31–51.

Butterworth, N.P., Talsma, A.S., Müller, R.D., Seton, M., Bunge, H.P., Schuberth, B.S.A., Shephard, G.E. and Heine, C., 2014. Geological, tomographic, kinematic and geodynamic constraints on the dynamics of sinking slabs. Journal of Geodynamics, 73, pp.1-13.

Chase, C.G., 1979. Subduction, the geoid, and lower. Nature, 282, p.29.

Chase, C.G. and Sprowl, D.R., 1983. The modern geoid and ancient plate boundaries. Earth and Planetary Science Letters, 62(3), pp.314-320.

Christensen, U.R. and Yuen, D.A., 1985. Layered convection induced by phase transitions. Journal of Geophysical Research: Solid Earth, 90(B12), pp.10291-10300.

Christensen, U.R., 1996. The influence of trench migration on slab penetration into the lower mantle. Earth and Planetary Science Letters, 140(1-4), pp.27-39.

Čížková, H., van Hunen, J., van den Berg, A.P. and Vlaar, N.J., 2002. The influence of rheological weakening and yield stress on the interaction of slabs with the 670 km discontinuity. Earth and Planetary Science Letters, 199(3), pp.447-457.

Dziewonski, A.M., 1984. Mapping the lower mantle: determination of lateral heterogeneity in P velocity up to degree and order 6. Journal of Geophysical Research: Solid Earth, 89(B7), pp.5929-5952.

Flament, N., Gurnis, M., Williams, S., Seton, M., Skogseid, J., Heine, C. and Müller, R.D., 2014. Topographic asymmetry of the South Atlantic from global models of mantle flow and lithospheric stretching. Earth and Planetary Science Letters, 387, pp.107-119.

Ghosh, A., Thyagarajulu, G. and Steinberger, B., 2017. The Importance of Upper Mantle Heterogeneity in Generating the Indian Ocean Geoid Low. Geophys. Res. Lett.

Gibbons, A.D., Zahirovic, S., Müller, R.D., Whittaker, J.M. and Yatheesh, V., 2015. A tectonic model reconciling evidence for the collisions between India, Eurasia and intra-oceanic arcs of the central-eastern Tethys. Gondwana Res., 28(2), 451-492.

Gurnis, M. and Hager, B.H., 1988. Controls of the structure of subducted slabs. Nature, 335(6188), 317-321.

Gurnis, M., Mitrovica, J.X., Ritsema, J. and van Heijst, H.J., 2000a. Constraining mantle density structure using geological evidence of surface uplift rates: The case of the African superplume. Geochem. Geophys. Geosyst., 1(7).

Gurnis, M., Ritsema, J., Van Heijst, H.J. and Zhong, S., 2000b. Tonga slab deformation: The influence of a lower mantle upwelling on a slab in a young subduction zone. Geophys. Res. Lett., 27(16), 2373-2376.

Hafkenscheid, E., Wortel, M.J.R. and Spakman, W., 2006. Subduction history of the Tethyan region derived from seismic tomography and tectonic reconstructions. J. Geophys. Res., Solid Earth, 111(B8).

Hager, B.H., Clayton, R.W., Richards, M.A., Comer, R.P. and Dziewonski, A.M., 1984. Lower mantle heterogeneity, dynamic topography and the geoid.

Hall, R., 2012. Late Jurassic–Cenozoic reconstructions of the Indonesian region and the Indian Ocean. Tectonophysics, 570, 1-41.

Ishii, M. and Tromp, J., 1999. Normal-Mode and Free-Air Gravity Constraints on Lateral Variations in Velocity and Density of Earth's Mantle. Science, 285(5431), 1231-1236.

Jarvis, G.T. and Lowman, J.P., 2007. Survival times of subducted slab remnants in numerical models of mantle flow. Earth Planet. Sci. Lett. 260(1), 23-36.

King, S.D., Frost, D.J. and Rubie, D.C., 2015. Why cold slabs stagnate in the transition zone. Geology, 43(3), pp.231-234.

Koelemeijer, P., Deuss, A. and Ritsema, J., 2017. Density structure of Earth's lowermost mantle from Stoneley mode splitting observations. Nature Communications, 8.

Lau, H.C.P., Mitrovica, J.X., Davis, J.L., Tromp, J., Yang, H.Y., Al-Attar, D., 2017. Tidal tomography constrains Earth's deep-mantle buoyancy. Nature 551, 321–326.

Li, P., Rui, G., Cui, J., Ye, G., 2004. Paleomagnetic analysis of eastern Tibet: implications for the collisional and amalgamation history of the Three Rivers Region, SW China. J. Asian Earth Sci. 24, 291–310.

Li, Z., Ding, L., Lippert, P.C., Song, P., Yue, Y. and van Hinsbergen, D.J., 2016. Paleomagnetic constraints on the Mesozoic drift of the Lhasa terrane (Tibet) from Gondwana to Eurasia. Geology, 44(9), 727-730.

Lithgow-Bertelloni, C. and Silver, P.G., 1998. Dynamic topography, plate driving forces and the African superswell. Nature, 395(6699), 269-272.

Masters, G., Laske, G., Bolton, H. and Dziewonski, A., 2000. The relative behavior of shear velocity, bulk sound speed, and compressional velocity in the mantle: implications for chemical and thermal structure. Earth's deep interior: mineral physics and tomography from the atomic to the global scale, 63-87.

McNamara, A.K. and Zhong, S., 2004. The influence of thermochemical convection on the fixity of mantle plumes. Earth Planet. Sci. Lett., 222(2), 485-500.

Nerlich, R., Colli, L., Ghelichkhan, S., Schuberth, B. and Bunge, H.P., 2016. Constraining central Neo-Tethys Ocean reconstructions with mantle convection models. Geophys. Res. Lett. 43(18), 9595-9603.

Nyblade, A.A. and Robinson, S.W., 1994. The african superswell. Geophys. Res. Lett. 21(9), 765-768.

Schellart, W.P., Kennett, B.L.N., Spakman, W. and Amaru, M., 2009. Plate reconstructions and tomography reveal a fossil lower mantle slab below the Tasman Sea. Earth Planet. Sci. Lett. 278(3), 143-151.

Schubert, G., Turcotte, D.L. and Olson, P., 2001. Mantle convection in the Earth and planets. Cambridge University Press. 940.

Seton, M., Müller, R.D., Zahirovic, S., Gaina, C., Torsvik, T., Shephard, G., Talsma, A., Gurnis, M., Turner, M., Maus, S. and Chandler, M., 2012. Global continental and ocean basin reconstructions since 200Ma. Earth-Sci. Rev. 113(3), pp.212-270.

Simmons, N.A., Myers, S.C., Johannesson, G., Matzel, E., Grand, S.P., 2015. Evidence for long-lived subduction of an ancient tectonic plate beneath the southern Indian Ocean. Geophys. Res. Lett. 42, 9270–9278.

Spasojevic, S., Liu, L. and Gurnis, M., 2009. Adjoint models of mantle convection with seismic, plate motion, and stratigraphic constraints: North America since the Late Cretaceous. Geochem. Geophys. Geosyst. 10(5).

Spasojevic, S., Gurnis, M., Sutherland, R., 2010. Mantle upwellings above slab graveyards linked to the global geoid lows. Nat. Geosci. 3, 435–438.

Su, W.J. and Dziewonski, A.M., 1997. Simultaneous inversion for 3-D variations in shear and bulk velocity in the mantle. Physics of the Earth Planet. Interiors, 100(1-4), pp.135-156.

Solomatov, V.S. and Reese, C.C., 2008. Grain size variations in the Earth's mantle and the evolution of primordial chemical heterogeneities. J Geophys. Res., Solid Earth, 113(B7).

Torsvik, T.H., Burke, K., Steinberger, B., Webb, S.J. and Ashwal, L.D., 2010. Diamonds sampled by plumes from the core-mantle boundary. Nature, 466(7304), pp.352-355.

Zahirovic, S., Müller, R.D., Seton, M., Flament, N., Gurnis, M. and Whittaker, J., 2012. Insights on the kinematics of the India-Eurasia collision from global geodynamic models. Geochem. Geophys. Geosyst. 13(4).

Zahirovic, S., Seton, M. and Müller, R.D., 2014. The Cretaceous and Cenozoic tectonic evolution of Southeast Asia. Solid Earth, 5(1), p.227.

Zahirovic, S., Matthews, K.J., Flament, N., Müller, R.D., Hill, K.C., Seton, M. and Gurnis, M., 2016. Tectonic evolution and deep mantle structure of the eastern Tethys since the latest Jurassic. Earth-Science Rev. 162, 293-337.

Zhong, S. and Gurnis, M., 1995. Mantle convection with plates and mobile, faulted plate margins. Science, 838-838.

Zhong, S., Zuber, M.T., Moresi, L. and Gurnis, M., 2000. Role of temperature-dependent viscosity and surface plates in spherical shell models of mantle convection. J. Geophys. Res., Solid Earth, 105(B5), pp.11063-11082.

Zhu, D.C., Zhao, Z.D., Niu, Y., Mo, X.X., Chung, S.L., Hou, Z.Q., Wang, L.Q. and Wu, F.Y., 2011a. The Lhasa Terrane: Record of a microcontinent and its histories of drift and growth. Earth Planet. Sci. Lett., 301(1), pp.241-255.

Zhu, D.C., Zhao, Z.D., Niu, Y., Dilek, Y., Mo, X.X., 2011b. Lhasa terrane in Southern Tibet came from Australia. Geology 39, 727–730.

Van Der Meer, D.G., Spakman, W., Van Hinsbergen, D.J., Amaru, M.L. and Torsvik, T.H., 2010. Towards absolute plate motions constrained by lower-mantle slab remnants. Nature Geoscience, 3(1), 36-40.

Van der Voo, R., Spakman, W. and Bijwaard, H., 1999. Tethyan subducted slabs under India. Earth and Planetary Science Letters, 171(1), 7-20.

Yan, M., Zhang, D., Fang, X., Ren, H., Zhang, W., Zan, J., Song, C. and Zhang, T., 2016. Paleomagnetic data bearing on the Mesozoic deformation of the Qiangtang Block: implications for the evolution of the Paleo-and Meso-Tethys. Gondwana Res., 39, 292-316.

Figure captions

Figure 1. Slab-shaped seismic anomaly in the LLNL-G3D-JPS model (Simmons et al., 2015). (a) A cross section of the mantle between the Kerguelen Plateau to Indonesia shows a high shear-wave velocity anomaly (SEIS) dipping northward extending from the upper mantle to the CMB. The profile of the cross section is shown in Figure 1b. The start and end points of the cross section locate at 60°S, 43°E, and 0°S,113°E, respectively. In this cross-section, the African LLSVP is located below the SEIS anomaly. (b) Spatial distributions of SEIS anomaly at depths of 623 km, 871 km, 1,071 km, 1,671 km, 2,071 km and 2,471 km. The African LLSVP below the southern Indian Ocean is shown at depth of 2,471 km.

Figure 2. Tectonic reconstructions of the Lhasa terrane. (a) Map views of the Lhasa terrane northward drift (modified after Li et al., 2016). The paleolatitude of the Lhasa terrane is derived from paleomagnetic data, whereas the paleolongitude is unconstrained. The background is the plate reconstruction model of Zahirovic et al. (2016). Oceanic crustal ages are color-coded. (b) Schematic cross sections of the Mesozoic plate motions in the Indian Ocean region (modified after Zhu et al., 2011a). The northward migration of magmatism in the Lhasa terrane indicates a southward subducted Paleo-Tethyan plate below the northern Lhasa terrane, which gradually rolled back between 220 and 160 Ma. Meanwhile, the Meso-Tethyan Ocean opened as the trench retreated northward. A northward subduction of Meso-Tethyan ocean plate initiated at the southern margin of

Eurasia following final suturing of the Lhasa terrane with Qiangtang (160-115 Ma). ML = mantle lithosphere.

Figure 3. 2D model results at 160 Myr (from the start of model run). Left panel shows the thermal fields and right panel represents viscosity fields. (a) Model N20 with an initially north-dipping slab. Model S05 (b), Model S15 (c), and Model S17 (d) all have initially south-dipping slabs. The models shown in (a) and (b) have parameters that are otherwise identical except for the initial dip of the slab. The model shown in (c) has no excess viscosity in the pile compared to the nominal case in (b), while that shown in (d) has a larger increase in viscosity. Detailed model parameters are listed in Table S2. Initial model setup is shown in Fig. S2.

Figure 4. Initial temperature and viscosity profiles in Model 1. (a) Non-dimensional temperature profiles. (b) Viscosity structures. Black lines represent horizontally averaged values. Blue dashed lines represent mantle outside thermochemical piles. Red dashed lines denote the profiles that pass through thermochemical piles.

Figure 5. Initial setup of global mantle convection model. (a) Average temperature fields between 350-750 km depths. The dashed line shows the spatial extend of the upper portion of inserted slab. (b) Average temperature fields between 750-1,200 km depths. The dashed line shows the spatial extend of the lower portion of inserted slab. (c) The thermal field at 2,470 km depth. Two high-temperature anomalies are constructed to simulate the African and Pacific thermochemical piles. The spatial positions are generally

based on tomography observations. (d) The cross section of temperature and viscosity fields of mantle from the Kerguelen Plateau to Indonesia.

Figure 6. Result of Model 1 that shows the interaction between the synthetic Mesozoic subducted slab and the African pile below the southern Indian Ocean. Left column shows the plate reconstruction model of Zahirovic et al. (2016). Right column shows the cross section of the non-dimensional temperature field of mantle. Black line represents the extent of African thermochemical pile.

Figure 7. Temperature fields at the depths of 402 km, 791 km, 1,847 km and 2,470 km at 0 Ma in Model 1.

Figure 8. Summary of global model results and compare with the seismic observation. Contours represent mantle that is 10% lower than ambient mantle temperature caused by the subducted slabs. Model parameters are listed in Table 2. The time-dependent evolutions of mantle structures are shown in Figs. 6, S3 and S4. Background is LLNL-G3D-JPS model (Simmons et al., 2015).

Table 1 Invariant parameters in global models

Parameter	Value
Mantle density	3300 kg/m^3
Reference viscosity	10^{21} Pa s
Gravitational acceleration	9.8 m/s^2
Thermal expansion coefficient	3×10^{-5} C^{-1}
Thermal diffusivity	10^{-6} m^2/s
Reference temperature	2800 °C
Surface temperature	0 °C
Earth radius	6371 km
Mantle height	2867 km

Table 2. Summary of global models

Model	Lower mantle η_0	Clapeyron slope at 660 km discontinuity	Age of inserted Slab	Thermochemical piles		Slab polarity reverse	Figure
				Density increase	Viscosity η_c		
1	50	-2 MPa K^{-1}	40-80 Myr	100 kg/m^3	10	Y	Fig.6
2	50	-2 MPa K^{-1}	-	100 kg/m^3	10	-	Fig.S3a
3	50	-2 MPa K^{-1}	40-80 Myr	-	-	N	Fig.S3b
4	50	-2 MPa K^{-1}	80-120 Myr	100 kg/m^3	10	Y	Fig.S3c
5	30	-2 MPa K^{-1}	40-80 Myr	100 kg/m^3	10	Y	Fig.S3d
6	50	-	40-80 Myr	100 kg/m^3	10	Y	Fig.S3e
7	50	-2 MPa K^{-1}	40-80 Myr	100 kg/m^3	1	Y	Fig.S4a
8	50	-2 MPa K^{-1}	40-80 Myr	125 kg/m^3	10	Y	Fig.S4b

Grey shading represents the parameter that is different from Model 1

Figure 1

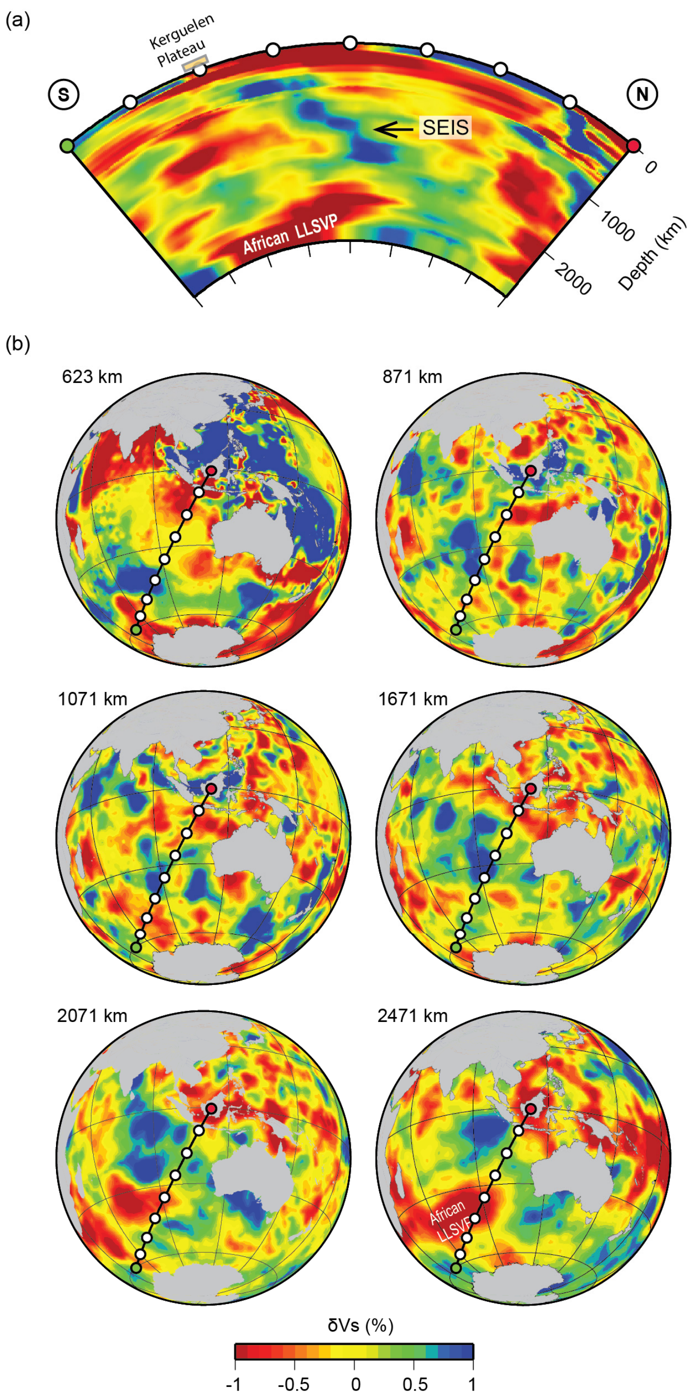
(a)
Kerguelen Plateau
S
N
SEIS
0
1000
2000
Depth (km)
African LLSVP
(b)
623 km
871 km
1071 km
1671 km
2071 km
2471 km
African LLSVP
δVs (%)
-1
-0.5
0
0.5
1

Figure 2

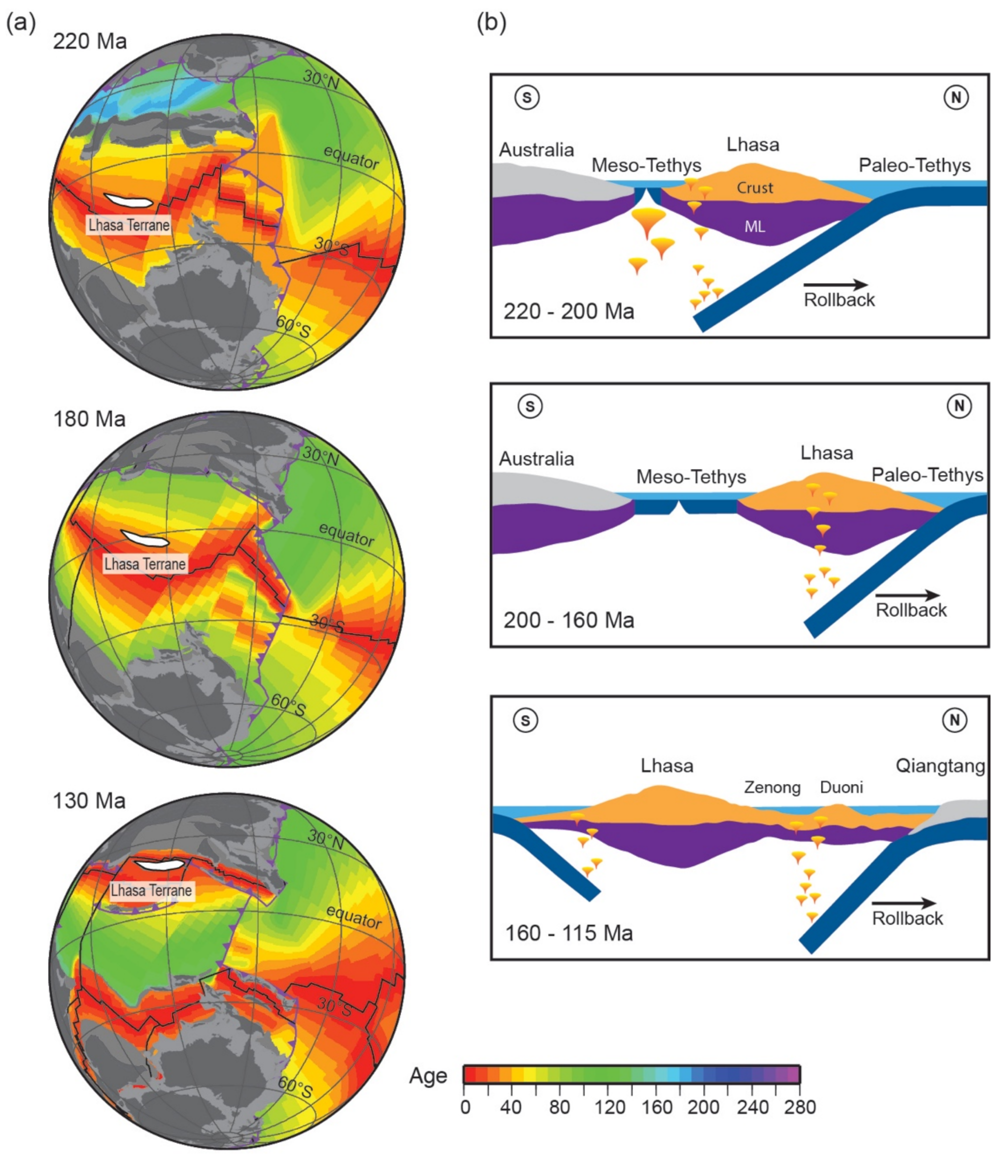
(a)
220 Ma
30°N
equator
Lhasa Terrane
30°S
60°S
180 Ma
30°N
equator
Lhasa Terrane
30°S
60°S
130 Ma
30°N
equator
Lhasa Terrane
30°S
60°S
Age
0 40 80 120 160 200 240 280
(b)
S
N
Australia
Meso-Tethys
Lhasa
Paleo-Tethys
Crust
ML
Rollback
220 - 200 Ma
S
N
Australia
Meso-Tethys
Lhasa
Paleo-Tethys
Rollback
200 - 160 Ma
S
N
Lhasa
Zenong
Duoni
Qiangtang
Rollback
160 - 115 Ma

628 **Figure 3**

629

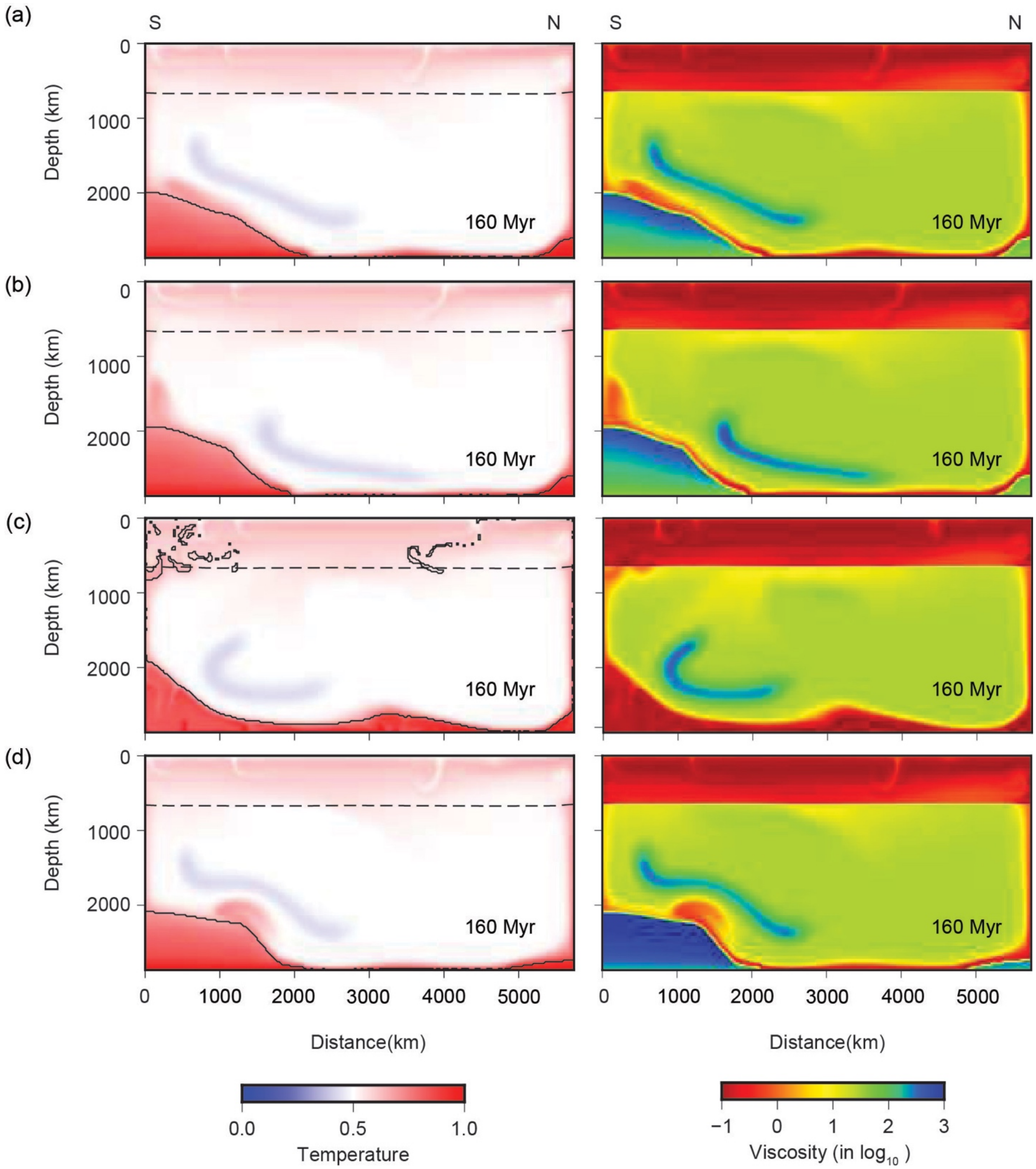

630

Figure 4

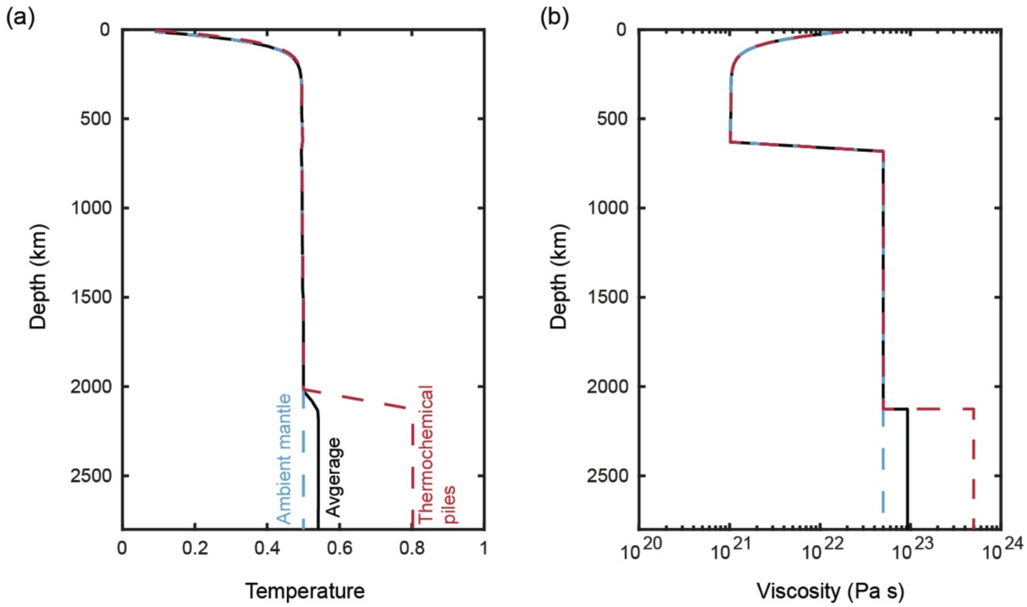
(a)
(b)
Depth (km)
Temperature
Viscosity (Pa s)
Ambient mantle
Avgerage
Thermochemical piles

Figure 5

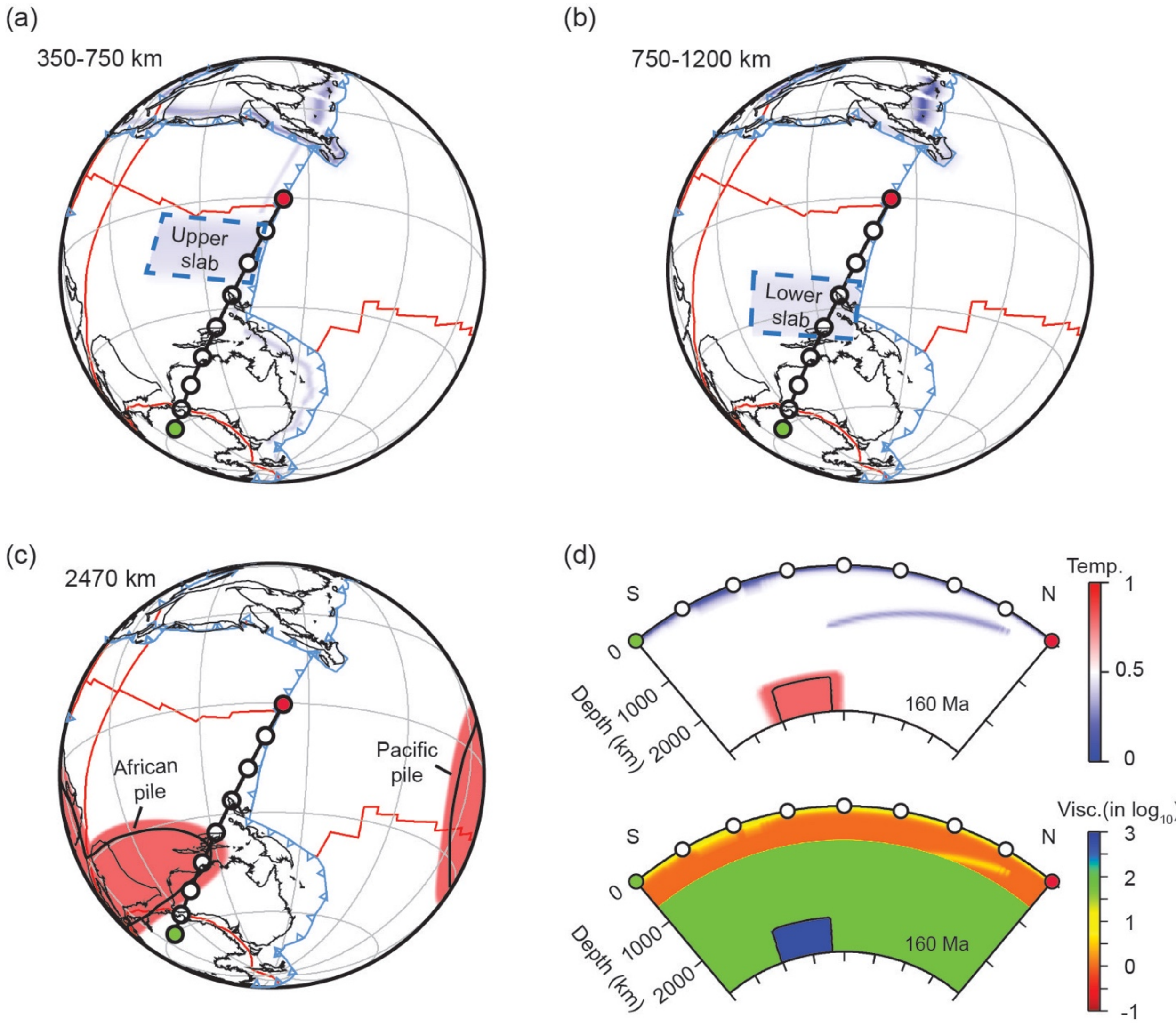
(a)
350-750 km
Upper slab
(b)
750-1200 km
Lower slab
(c)
2470 km
African pile
Pacific pile
(d)
S
N
Temp.
1
0.5
0
0
Depth (km) 1000 2000
160 Ma
Visc.(in log_{10})
3
2
1
0
-1

Figure 6

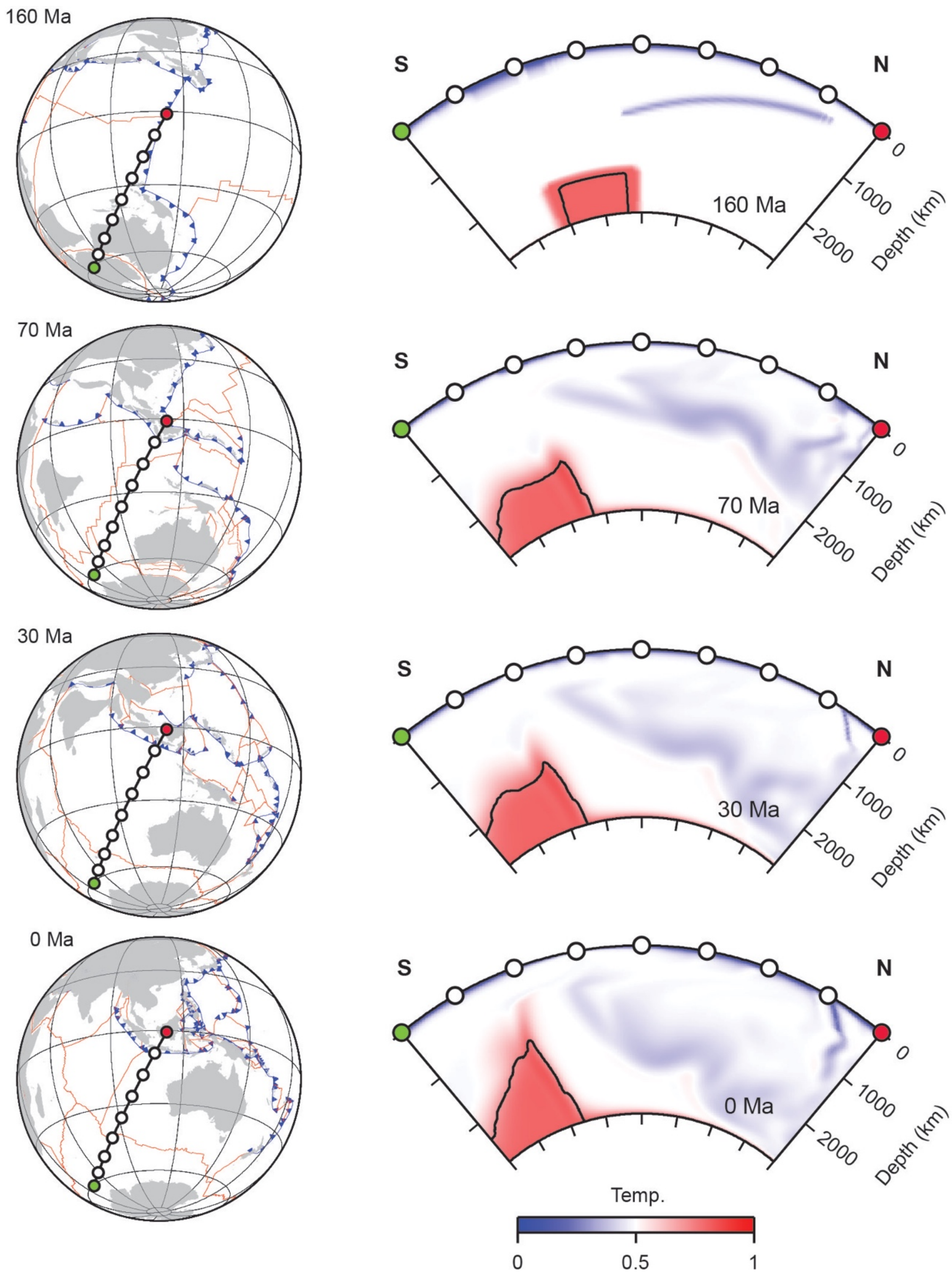
160 Ma
S
N
0
1000
2000
Depth (km)
160 Ma
70 Ma
S
N
0
1000
2000
Depth (km)
70 Ma
30 Ma
S
N
0
1000
2000
Depth (km)
30 Ma
0 Ma
S
N
0
1000
2000
Depth (km)
0 Ma
Temp.
0
0.5
1

Figure 7

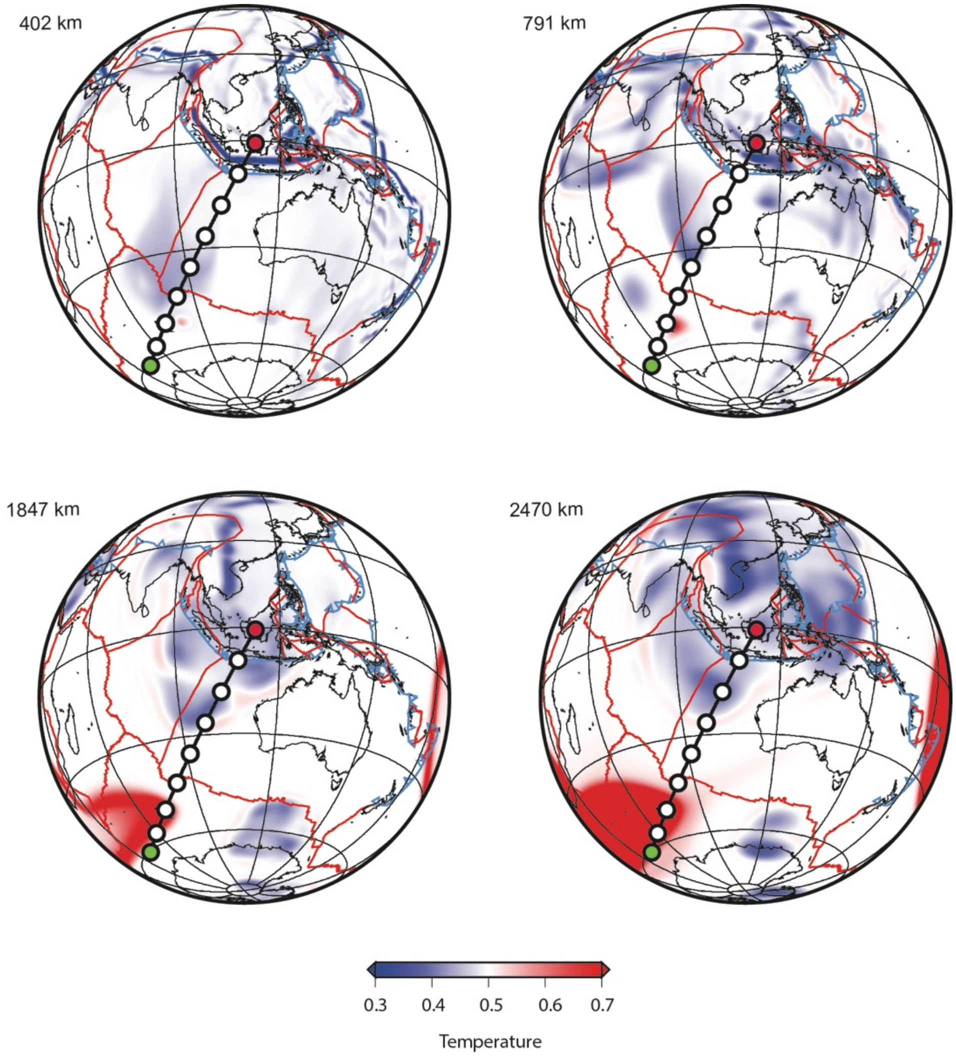

Figure 8

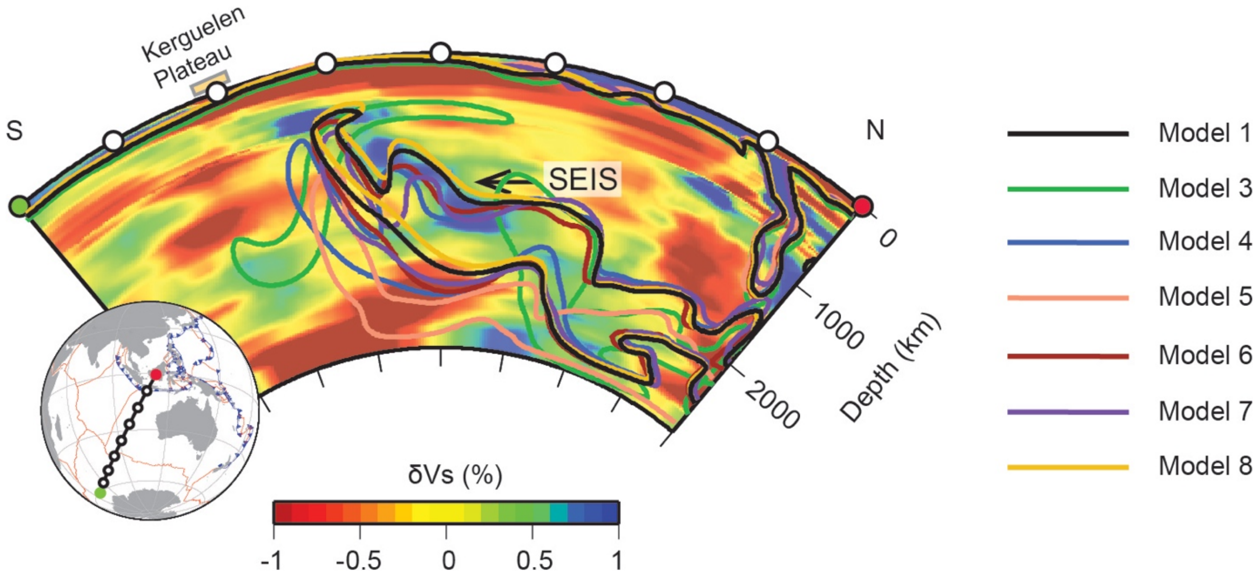
Kerguelen Plateau
S
N
SEIS
0
1000
2000
Depth (km)
δVs (%)
-1
-0.5
0
0.5
1
Model 1
Model 3
Model 4
Model 5
Model 6
Model 7
Model 8

Supplementary Material

1. Model setup for 2D models

We compute two-dimensional mantle convection models in a Cartesian coordinate system in which the equations are solved with code *Citcom2D* to solve mass, momentum and energy equations (Moresi and Solomatov, 1995). The model domain is 5,740 km × 2,870 km (horizontal × vertical) with 256×128 elements and 16 markers per element. The top and bottom boundaries are free-slip, and temperatures are set to be T=0.5 (non-dimensional) at the top and T=1 at the bottom boundaries. Besides the fundamental properties like the viscosity jump and Clapeyron slope at 660 km discontinuity, we also test the properties of the isolated slab and thermochemical piles in models.

The Rayleigh Number $Ra = \frac{\alpha\rho g\Delta T h^3}{\kappa\eta_r}$ of the ambient mantle equals 3.31×10^7 based on the buoyancy and viscosity parameters in the Table S1. For the Rayleigh number of the chemical pile ($\mathrm{Rc} = \frac{\Delta\rho g h^3}{\kappa\eta_r}$, where $\Delta\rho$ is the density contrast), we use the buoyancy number $\frac{\mathrm{Rc}}{\mathrm{Ra}}$ to describe the density difference between the thermochemical pile and ambient mantle (Table S2).

The viscosity in models depends on temperature, depth and composition:

$$\eta(\mathrm{T}) = \eta_0 \exp\left(\frac{\mathrm{E}}{\mathrm{T}^* + \mathrm{visT}} - \frac{\mathrm{E}}{0.5 + \mathrm{visT}}\right)$$

$$\eta(\mathrm{C},\mathrm{T}) = \eta(\mathrm{T}) \exp\left(\mathrm{C} \cdot \mathrm{lnViscc0}\right)$$

where $\mathrm{T}^* = \min[\max(\mathrm{T}, 0), 1]$, T is the non-dimensional temperature. η_0 is pre-factor for depth. $\eta_0 = 1$ for the upper mantle, and has different values for the lower mantle in different cases (see details in Table S2). In all models, visT equals 0, and E (active energy) equals 6.90. C is composition factor varying between 0 and 1. Viscc0 is the compositional dependent parameter, controlling the viscosity contrast between thermochemical pile and ambient mantle.

To approximate the temperature profile of the subducted slab, we use a Gaussian function to describe the cross section of the rectangular slab,

$$\mathrm{T} = 0.5 - \frac{1}{\sqrt{2\pi}} \mathrm{e}^{-\frac{\mathrm{x}^2}{\sigma^2}}$$

where x is the distance from the perpendicular bisector of the slab width. The standard deviation σ is always eighth of slab width, in order to cut off Gaussian curve in a proper length.

In a realistic slab, the temperature structure is not symmetrical, but similar to an error function in the situation of instantaneous cooling of a semi-infinite half-space, which relates to the age of oceanic lithosphere. When calculating the equivalent amount of buoyancy between a hypothetical slab and a realistic slab, the relationship between width and age of Gaussian slab can be obtained as

$$\int_{-\infty}^{+\infty} e^{-\frac{x^2}{2\sigma^2}} dx = \int_{0}^{+\infty} erfc(\frac{y}{2\sqrt{\kappa t}})\, dy$$

$$\sigma = \frac{width}{8}$$

60-Myr-old and 130-Myr-old hypothetical slabs correspond to the width value 0.0563 and 0.08, respectively.

For the temperature field of thermochemical piles, we connect initial temperature with its initial composition field. We apply a hyperbolic tangent function to construct the upper boundary ($Cline$) of the thermochemical piles

$$Cline(x) = \frac{in}{2} + \frac{h - in}{2}\{1 + \tanh[20(w - in - x)]\}$$

where we take in as 0.015. w is the width of the LLSVP, and h is the height of the LLSVP. The temperature field for the LLSVP is constructed as

$$T(x, z) = \frac{1}{2} + \frac{1}{4}\{1 + \tanh[5(z_0(x) - z)]\}$$

$$z_0(x) = in + \frac{h - in}{2}\{1 + \tanh[20(w - x)]\}$$

2. Viscosity structure in global models

In the global models, the viscosity depends on the temperature, depth and composition

$$\eta = \eta_r \eta_0 \eta_c exp\,[E \times (0.5 - T)]$$

where η_r is the reference viscosity listed in Table 1. η_0 is the non-dimensional viscosity prefactor depending on depths, with value equals to 1 in the lithosphere and upper mantle. The value of η_0 in lower mantle varies in models (listed in Table 2). η_c is the viscosity pre-factor depending on composition. The value of η_c of the thermochemical piles is listed in Table 2, and $\eta_c = 1$ for other materials. E is non-dimensional activation energy. E=7 in the upper mantle and equals zero in the lower mantle. T is non-dimensional temperature.

Table S1 Constant parameters in 2D models

Symbol	Description	Value
α	Thermal expansion coefficient	$2.5 \times 10^{-5} K^{-1}$
ρ	Density	$4 \times 10^{3}\ kg/m^{3}$
g	Gravity acceleration	$10\ m/s^{2}$
ΔT	Temperature contrast	$1400\ K$
h	Mantle depth	$2870\ km$
κ	Thermal diffusion constant	$10^{-6}\ m^{2}/s$
η_r	Reference viscosity	$10^{21} Pa \cdot s$